Research Article Vol. 34, No. 8 / 20 Apr 2026 / *Optics Express* 13882

Optics EXPRESS

Influence of zinc diffusion on the optical performance of heterogeneously integrated C-band lasers

MICHELE ZENARI,[1,*] BIWEI PAN,[1] JING ZHANG,[1] DELPHINE NEEL,[2] JOAN RAMIREZ,[2] AND GÜNTHER ROELKENS[1]

[1] *Photonics Research Group, Department of Information Technology (INTEC), Ghent University–imec, Ghent 9052, Belgium*
[2] *III-V Lab, Palisseau 91767, France*
[*] *Michele.Zenari@UGent.be*

Abstract: In this work, we investigate the impact of contact annealing on the device performance of C-band laser diodes micro-transfer printed onto a silicon photonics platform. Annealing allows reducing the contact resistance of the devices but can also have an impact on the diffusion of dopants towards the active region, decreasing the quantum efficiency of the laser. This trade-off is studied in this paper. Through capacitance deep-level transient spectroscopy (C-DLTS) analysis, the decrease in performance upon annealing is associated with zinc impurities. These defects are believed to diffuse toward the active region, and as a result, act as non-radiative recombination centers. To eliminate the influence of the micro-transfer printing step, two sets of devices were compared. Both were fabricated from the same epitaxial wafer and underwent identical processing, except that one set was characterized before transfer-printing on the native substrate, whereas the other was measured after being transfer-printed onto silicon. C-DLTS measurements confirmed that the same process occurs on native InP substrates. Once the device contacts are annealed, constant current stress testing does not introduce further substantial threshold current variations.

1. Introduction

The demand for data capacity and bandwidth has increased dramatically in recent years, driving the need for new solutions in information processing and communication [1] [2]. Silicon photonics (SiPh) has emerged as a promising platform that combines the scalability of CMOS manufacturing with the advantages of optical signal processing. Photonic integrated circuits (PICs) based on Si or SiN offer cost-effective production and energy-efficient operation, and are considered key enablers for next-generation data communication systems [3].

A major limitation of silicon is its indirect bandgap [4], which prevents efficient light emission and hinders the monolithic integration of lasers, one of the most critical components of PICs. To overcome this, the monolithic integration of III–V materials on silicon has been extensively investigated. However, the lattice and thermal expansion mismatch between silicon and III–V semiconductors leads to formation of crystalline defects and reduced device performance [5–7]. Various approaches have been explored to address this challenge, including quantum dot (QD) laser integration [8], which benefits from high defect tolerance, and selective area growth (SAG), which confines dislocations away from the active region [9]. Heterogeneous integration methods, such as wafer bonding [10] and flip-chip assembly [11], provide an alternative by growing III–V materials separately and subsequently integrating them onto silicon.

More recently, micro-transfer printing (μTP) [12] has emerged as a versatile heterogeneous integration technique. μTP enables the transfer of a wide range of pre-fabricated devices with sub-micron accuracy in a massively parallel manner, thereby overcoming lattice-matching

#585401 https://doi.org/10.1364/OE.585401
Journal © 2026 Received 17 Dec 2025; revised 20 Feb 2026; accepted 25 Feb 2026; published 7 Apr 2026

constraints while offering high throughput and scalability. This approach has shown strong potential for dense integration of III–V lasers onto SiPh platforms [13].

Evanescent coupling of III-V lasers to silicon photonics enables efficient optical interfacing over a broad wavelength range and with very low back-reflection. However, it requires epitaxial layer structures with thin n-contact layers to enable efficient optical coupling, as illustrated in Fig. 1. This thin contact layer requires that contact annealing, to reduce the series resistance of the device is in general best carried out after micro-transfer printing, as spiking of the n-metal contact through the n-contact layer into the release layer would hamper high yield printing. In this paper we assess the impact of this annealing on the device performance of C-band III-V-on-silicon Fabry-Perot lasers. As expected, a reduction in the series resistance can be observed, however, it is accompanied with a decrease in the quantum efficiency of the printed devices.

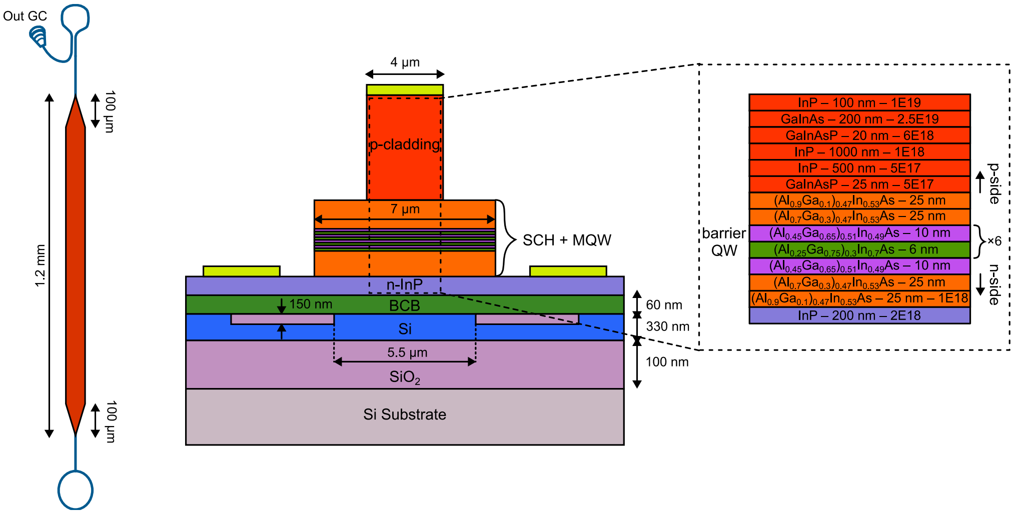

Fig. 1. Schematic representation of the devices under test. The left side depicts a top view of the III-V cavity and the waveguide underlying it. The right side shows a cross-section of the device, highlighting the III-V epitaxial layer structure.

Through capacitance deep-level transient spectroscopy (C-DLTS), we identify zinc diffusion as a key factor contributing to defect-induced quantum efficiency reduction. Finally, by comparing native InP and µTP-integrated devices, we demonstrate that the µTP process itself is not responsible for the observed changes in device performance.

Thanks to these results, we can state that the micro-transfer printing integration does not affect the quality of the III-V material. Therefore, µTP is a promising candidate for integrating III-V devices in large-volume silicon photonics production. Lastly, we demonstrated that the origin of the initial stabilization of the optical performance can be addressed using non-destructive characterization techniques (C-DLTS), which could be exploited in the future for statistical analysis on a wafer scale.

2. Devices under test

The devices investigated in this work are InP Fabry–Perot laser diodes integrated onto a silicon platform via micro-transfer printing using a benzocyclobutene (BCB) adhesion layer. Beyond providing mechanical adhesion, the BCB layer has a crucial impact on device performance. It not only planarizes the surface topography but, more importantly, defines the vertical separation between the III–V active region and the silicon waveguide, thereby directly influencing the optical coupling efficiency. In addition, its relatively low Young’s modulus helps relieve thermomechanical stress between the heterogeneous materials. Finally, because of its low thermal conductivity, the BCB thickness strongly affects heat dissipation from the active device. The samples are designed for operation at an emission wavelength of about 1.55 µm. The laser structure, illustrated in Fig. 1, consists of an active region enclosed by p-InP cladding layers, doped with zinc and an 200 nm thick n-InP region doped with silicon (n-side). The active region comprises six identical AlGaInAs quantum wells (QWs). The laser emission is coupled into an underlying Si/SiO_2 waveguide using adiabatic taper structures. The mesa width is 4 µm, while the width of the separate confinement heterostructure (SCH) and active region is 7 µm. The cavity length is 1.2 mm, which includes the two 100 µm long adiabatic tapers at the ends. Optical feedback is provided by silicon loop mirrors located at both ends of the waveguide, with reflectivities of ≈40% and 100%, implemented in the 330 nm thick silicon device layer. The output light is extracted through a grating coupler (GC). The III–V coupons are defined on an InP wafer by e-beam lithography and ICP etching of the mesa and taper structures, followed by hard-mask patterning to form isolated device islands. Tethers are realized by SiNx deposition and RIE, providing mechanical support during selective $FeCl_3$ wet etching of the release layer, which undercuts the InP substrate to suspend the coupons; a photoresist encapsulation layer is applied prior to release to reinforce the tethers. The released coupons are retrieved using a PDMS-based stamp in an X-Celeprint µTP-100 system and deterministically aligned to Si waveguide recesses prepared by RIE and BHF etching. A BCB layer is spray-coated and soft-baked prior to printing to promote adhesion, followed by a post-print oxygen plasma clean and final metallization to complete electrical interconnection. Further details on device processing and design can be found in [14].

3. Impact of annealing on device performance

After device fabrication and micro-transfer printing, the lasers underwent an annealing step. This process is common in compound semiconductor devices, as it is widely used to improve contact resistance and consequently reduce the overall series resistance [15]. The devices investigated in this study were annealed at 300 °C for 60 seconds. The annealing step was carried out by a rapid thermal annealing system in vacuum (both ramp up and cool down rates were 10°C/s). Figure 2 compares the electrical (series resistance) and optical (threshold current) performance before and after annealing. The series resistance decreased by approximately 1 Ω (i.e. almost by 15%), consistent with the expected improvement in contact resistance due to interdiffusion between

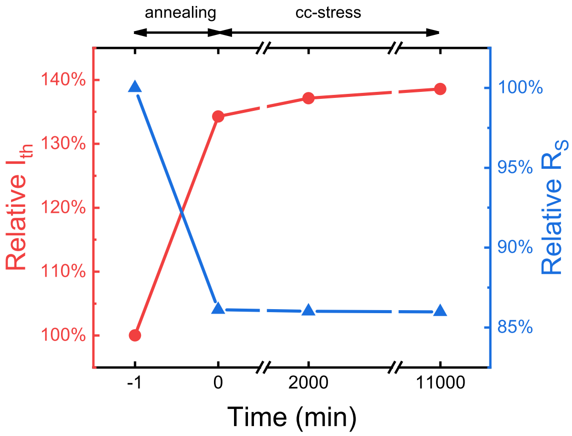

Fig. 2. Optical and electrical performance variation due to annealing (from -1 to 0 min) and afterwards during constant-current stress (from 0 to 11000 min).

the metal layers and the semiconductor surface [16,17]. However, a simultaneous increase in threshold current was observed (≈ + 10 mA). Subsequently, the devices were subjected to a constant-current stress test (150 mA, 25 °C) to assess their stability. After 11,000 minutes of stress (about one week), the devices exhibited a slight further reduction in series resistance (−0.5% relative to the pre-annealing value) and a small increase in threshold current (+3% relative to the pre-annealing value).

4. Assessment of threshold increase mechanism

In order to properly assess the mechanism resulting in the laser threshold increase, additional devices were subjected to constant-current stress without undergoing any contact annealing step. The goal of this measurement is to slow down the degradation effect allowing additional analysis using DLTS. The devices were aged again under a constant current of 150 mA (≈ 4 kA/cm^2) at an ambient temperature of 25 °C. Based on combined thermal simulations and experimental measurements of the devices' thermal impedance, the internal temperature under stress conditions is estimated to be approximately 75 °C. Notably, the same increase in threshold current observed after annealing (≈ + 10-11 mA) was reached during this new experiment after approximately 1000 minutes of stress, attributed to self-annealing of the devices. The resulting worsening of the L–I characteristics is shown in Fig. 3. The light–current curves exhibit an increase in threshold current (I$_{th}$), accompanied by a decrease in slope efficiency (SE) and in the optical power below threshold (OP$_{sub}$).

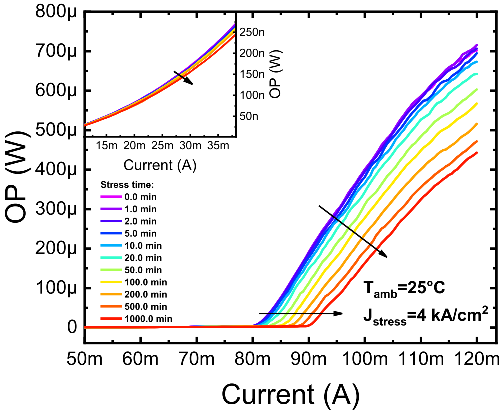

Fig. 3. L-I characteristics measured during a constant current stress (I$_{stress}$=150 mA). The unaged threshold is about 80 mA. The graph on the top-left corner depicts the optical power measured below threshold.

To analyze the observed performance reduction, the relative threshold current was plotted as a function of the relative OP$_{sub}$. Figure 4(a)) shows a linear correlation between the relative variations of I$_{th}$ and OP$_{sub}$ during the stress test. The relationship can be analyzed using the following theoretical expressions [18]:

$$I_{th} = \frac{qVN_{th}}{\eta_{inj}\tau} = \frac{qV(A + BN_{th} + CN_{th}^2)N_{th}}{\eta_{inj}} \tag{1}$$

$$OP_{sub} \propto \eta_r = \frac{BN^2}{BN^2 + AN + CN^3} \tag{2}$$

where q is the elementary charge, V is the active region volume, η_{inj} is the injection efficiency, τ is the carrier lifetime, N is the carrier density (N$_{th}$ at threshold), and A, B, and C are the

Shockley–Read–Hall (SRH), bimolecular, and Auger recombination coefficients, respectively. Both I_{th} and OP_{sub} depend on the balance between the radiative (BN^2) and non-radiative recombination terms ($AN+CN^3$). Assuming that the variation of the Auger term (CN^3), caused by the increase in carrier density N_{th} during stress, is smaller than the corresponding increase in Shockley–Read–Hall (SRH) recombination (A coefficient), the observed linear correlation indicates an enhancement of defect-related recombination within the device. This increase in A coefficient leads to the simultaneous variation of I_{th} and OP_{sub}.

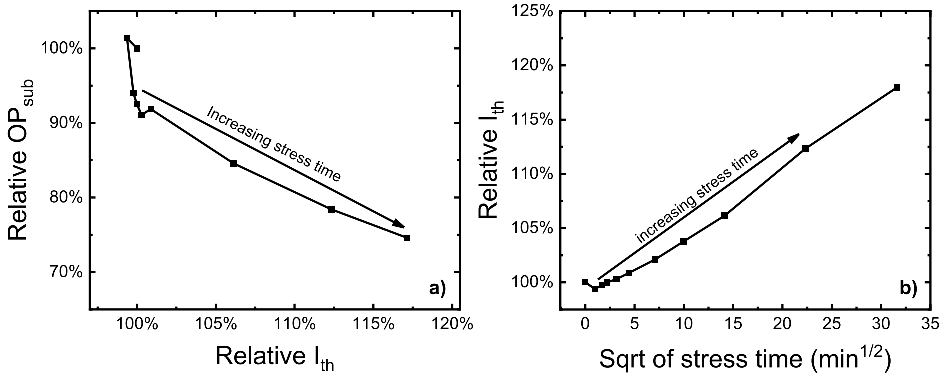

Fig. 4. a) correlation between I_{th} and OP_{sub}. b) I_{th} degradation as a function of the square root of time.

Figure 4(b)) presents the evolution of I_{th} as a function of the square root of stress time, revealing a linear dependence. This behavior can be interpreted in terms of Fick's second law of diffusion. When impurities diffuse from a region with constant surface concentration N_0, the impurity concentration N(x,t) at a given depth x and time t can be expressed as:

$$N(t,x) = \frac{N_0}{\sqrt{4\pi Dt}} e^{-\frac{x^2}{4Dt}} \tag{3}$$

where D is the diffusion coefficient of the migrating species. Because the density of diffusing non-radiative recombination centers (NRRCs) directly affects the non-radiative lifetime τ_{nr} (dominated by SRH recombination), a square-root time dependence of τ_{nr} reduction is expected. These observations indicate that the device performance change is governed by a diffusion-driven process that increases non-radiative recombination, changing the quantum efficiency of the laser.

5. Deep-level characterization

5.1. Deep level transient spectroscopy

In the previous section, we hypothesized that the observed optical variation was driven by an increase in non-radiative recombination centers near the active region. To characterize these defects, capacitance deep-level transient spectroscopy (C-DLTS) was employed. This technique measures capacitance transients as a function of temperature to determine the thermal emission behavior of defect states. For these measurements, an impedance analyzer was used to apply a square-wave voltage signal to the device and measure the resulting small-signal capacitance as a function of time. During the filling pulse (t_p), when the voltage V_{fill} is applied, the defects inside the semiconductor capture carriers. During the subsequent measurement pulse, under the voltage V_{meas}, these carriers are thermally emitted. The resulting capacitance transient exhibits an exponential trend, from which defect-related parameters can be extracted. Further details on the DLTS technique can be found in [19].

Figure 5(a)) shows representative capacitance transients recorded over a range of temperatures. From these experimental data, the transients were fitted to extract the emission rate e_n as a function of temperature. According to the standard expression for the emission rate, the corresponding Arrhenius relation can be written as [20]:

$$e_n = \gamma T^2 \sigma_\infty e^{-\frac{qE_a}{kT}} \Rightarrow \ln\left(\frac{T^2}{e_n}\right) = \frac{qE_a}{kT} + \ln\left(\frac{1}{\gamma\sigma_\infty}\right) \tag{4}$$

where T is the device temperature, k is the Boltzmann constant, σ_∞ is the apparent capture cross-section, and E_a is the activation energy. The term γ is defined as $\gamma = 2\sqrt{3}(2\pi)^{3/2}k^2m^*h^{-3}$, where h is the Planck's constant and m* is the effective mass of the charge carriers. From the experimental Arrhenius plot (where $\tau = e_n^{-1}$) shown in Fig. 5(b)) two defect signatures were identified, labeled T_1 (E_a≈0.40 eV) and T_2 (E_a≈0.5 eV).

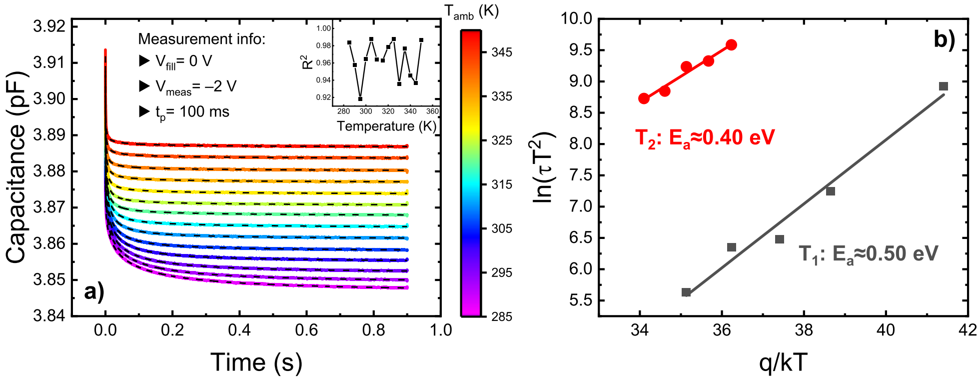

Fig. 5. a) capacitance transients captured between 285 K and 350 K applying V_{fill}=0 V, V_{meas}=–2 V, and t_p = 100 ms, together with the corresponding fits (dashed curves). The top-right inset shows the fit quality assessed via the R^2 coefficient. b) Arrhenius plot extrapolated from a). The data was fitted with a double exponential function [$y = y0 + A_1\exp(-t/\tau_1) + A_2\exp(-t/\tau_2)$] to discern the two defects.

The Arrhenius plot provides a unique signature for identifying deep-level defects. To determine the physical origin of the two detected traps, the Arrhenius signatures of T_1 and T_2 were compared with those reported in the literature. For this purpose, an Arrhenius plot database was developed, collecting Arrhenius plots from previously published studies on InP-based materials. The results of this comparison are presented in Fig. 6(a)) and Fig. 6(b)). Trap T_1 exhibits matches with the antisite defect P_{In} [21–23] and with Zn-related deep levels [24]. Regarding trap T_2 we observed a few occurrences consistent with a Zn-impurity-related trap [25–27]. By further comparing the capture cross sections of the identified defects, T1: $(7 \pm 4) \times 10^{-17}$ cm², T2: $(9 \pm 7) \times 10^{-19}$ cm², we can state that T2 more closely resembles H1 ($\sigma \approx 7 \times 10^{-18}$ cm²) and H2 ($\sigma \approx 1 \times 10^{-18}$ cm²) in [25]. In contrast, the cross section of T1 appears more compatible with those reported in [22] ($\sigma = 1 \times 10^{-16}$ cm²) and [24] ($\sigma = 4 \times 10^{-16}$ cm²).

5.2. Capture kinetics

The results presented in the previous section suggest that the defect levels detected by DLTS are most likely associated with point defects rather than extended defects or dislocations. To verify this hypothesis, we performed a characterization analogous to DLTS, namely the capture kinetics. In contrast to DLTS, this method is conducted at a fixed temperature while varying the filling pulse duration t_p. This approach does not affect the thermal emission rate, since the temperature remains constant, but it does influence the transient amplitude. Specifically, longer

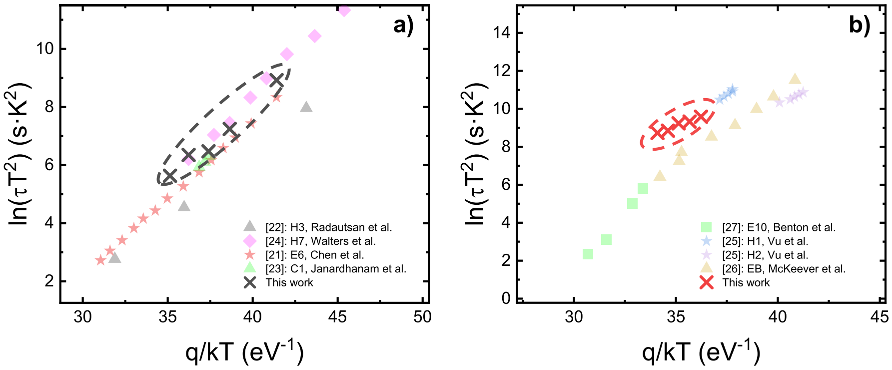

Fig. 6. Arrhenius plot comparison: a) defect T1, b) defect T2.

filling times lead to higher defect occupancy and, consequently, larger capacitance transients during carrier emission [28]. By analyzing the dependence of the transient amplitude on the filling pulse duration, it is possible to distinguish whether the observed defects correspond to non-interacting point defects or extended defects. For a non-interacting point defect, the carrier capture follows:

$$n_T\ (t_p)\ = N_T + [n_T(0) - N_T]\exp(-c_n t_p) \tag{5}$$

whereas for an extended defect, the relation is given by:

$$n_T\ (t_p)\ =\ c_n \tau N_T \ln\left(\frac{t_p}{\tau}\right) \tag{6}$$

Here, N_T is the total defect density, n_T is the trap occupancy as a function of the filling pulse duration t_p, c_n is the capture rate, and τ represents a characteristic time required for charge capture. The experimental results shown in Fig. 7 reveal that both T_1 and T_2 exhibit an exponential dependence on the filling pulse duration. This confirms that the two defect levels originate from non-interacting point defects rather than from dislocations or clusters of defects.

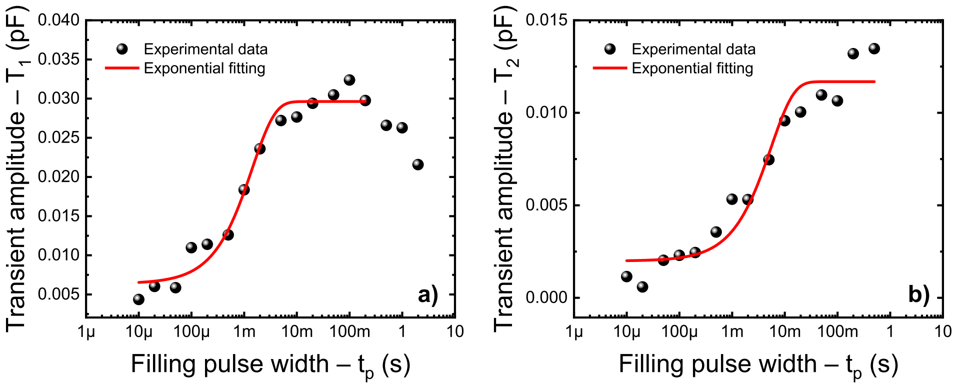

Fig. 7. Transient amplitude as a function of filling pulse width at 300 K for a) trap T_1 and b) trap T_2.

6. Defect density variation during stress

In the previous sections, we identified two deep levels present in the unaged devices. Their characteristics suggest a point-defect nature, most likely associated with Zn-related deep levels.

Even though Zn should act as a shallow acceptor (when substitutes In), it is well-known in the literature to generate defects during the interstitial-substitutional kick-out mechanism. Indeed Zn can either become an interstitial defect [29] or give rise to a zinc-phosphorus vacancy deep level [30]. To verify whether these defects are responsible for the observed threshold current shift, we characterized the trap density at different stages of the constant-current stress test. The defect concentration was determined through analysis of the DLTS transients. The trap density, N_T, can be expressed as [20]:

$$N_T \cong 2N_s \cdot \frac{\Delta C}{C_\infty} \tag{7}$$

Here, ΔC represents the capacitance transient amplitude, C_∞ is the steady-state capacitance, and N_s is the free carrier density obtained from C–V measurements. Figure 8 illustrates the correlation between threshold current increase and the trap densities of T_1 and T_2. The graph reveals two distinct phases. During the initial stage of stress (Ph1), no clear correlation is observed, as the threshold current exhibits minimal variation. At the same time, the trap density of T_2 increases, while that of T_1 shows only a slight change. After approximately 10 minutes of stress (Ph2), a strong correlation emerges between I_{th} increase and the increase in defect density. The trap density of T_2 rises from approximately 7×10^{14} cm^{-3} to 1.5×10^{15} cm^{-3}, whereas T_1 increases from about 6.5×10^{15} cm^{-3} to 8×10^{15} cm^{-3}.

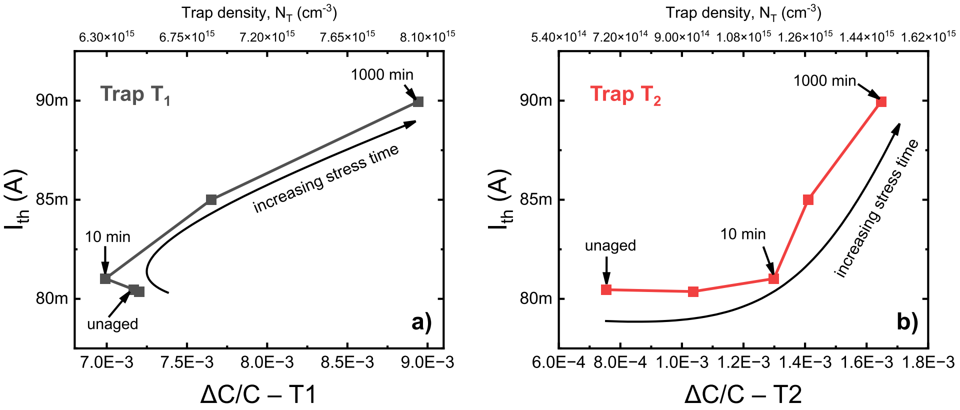

Fig. 8. Correlation between $\Delta C/C$ ratio (trap density) and optical degradation for a) trap T_1 and b) trap T_2.

Since both defects exhibit variation during stress and appear to be associated with Zn impurities, we modeled the degradation mechanism as illustrated in Fig. 9. The figure presents a simplified p–i–n junction representing the laser under investigation. In the p- and n-type regions the DLTS probing zones are highlighted, i.e. the semiconductor regions probed during the DLTS pulses described in the previous section. The DLTS probing region in the p-cladding is broader and located farther from the active region compared to that on the n-side. This results from the lower doping concentration in the p-cladding compared to the n-region. During Ph1, we hypothesize that Zn atoms begin diffusing from the p-cladding toward the active region. However, at this early stage, the diffusing species have not yet reached the active region; nevertheless, a variation in trap density (particularly for T_2) is detected, as the DLTS probing region extends slightly beyond the active layers. In contrast, during Ph2, the Gaussian diffusion tail, described by Fick's second law of diffusion (Eq. (3)), reaches the active region, resulting in the observed correlation between optical variation and defect concentration.

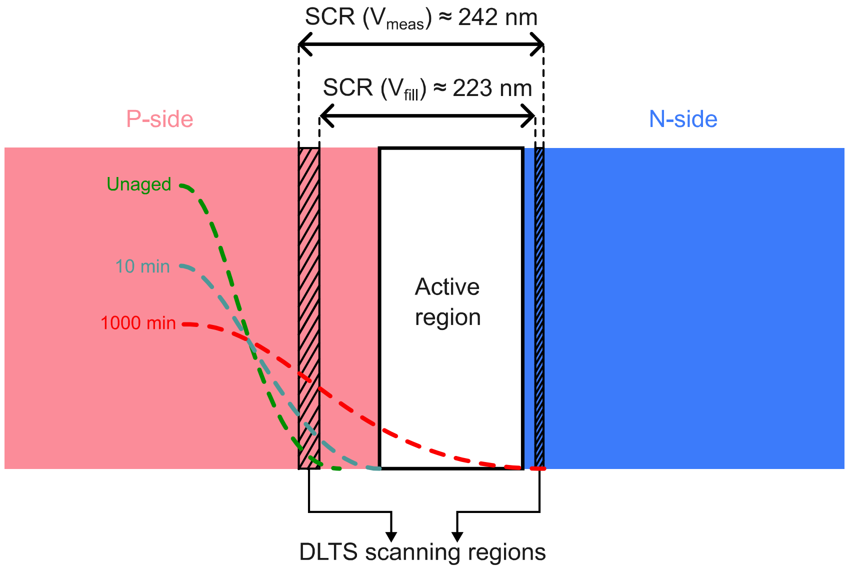

Fig. 9. Schematic representation of the degradation process. The Gaussian distributions represent Zn-related deep levels probed by DLTS. During Phase 1 ($t < 10$ min), the defects have not yet diffused into the active region. In Phase 2 ($t > 10$ min), the deep levels reach the active layers, inducing optical worsening.

7. On-source vs. on-target laser comparison

To ensure that the observed optical alteration during stress does not originate from the micro-transfer printing process, we compared two new sets of laser diodes fabricated from the same epitaxial wafer. Part of the III–V material was used to fabricate µTP laser diodes on a silicon platform (referred to as on-target devices), while the remaining material was used to fabricate Fabry–Perot (FP) lasers on the native substrate (on-source devices). DLTS measurements were performed again, and the Arrhenius plots in Fig. 10 show that the same two traps were also detected in the on-source devices. This comparison confirms that the identified defects do not originate from the transfer-printing processing but are already present in the III–V material. Therefore, the hypothesis of Zn-related defects appears well supported.

Finally, we compared the variation in trap density for both devices under the same aging conditions as described in the previous sections, namely a constant-current stress at $J = 4\,\mathrm{kA/cm^2}$ and $T_{amb} = 25°C$. The kinetics shown in Fig. 11 indicate that, similar to the results discussed in Section 6, the $\Delta C/C$ ratio (representing the trap density) increases with stress time. The device fabricated on the native substrate exhibits a faster kinetics, which can be explained by differences in thermal impedance. Specifically, the thermal conductivity of the InP substrate (on-source devices) is lower than that of silicon (on-target devices).

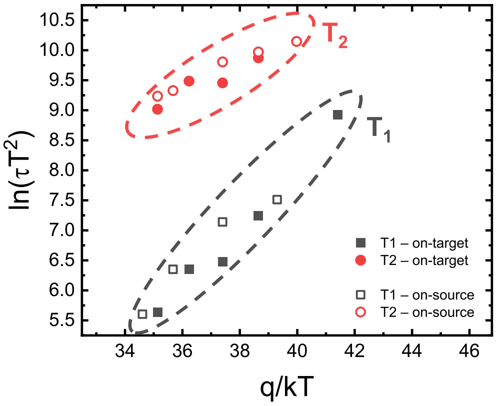

Fig. 10. Arrhenius plot comparison: on-source vs. on target. The same Arrhenius plot signatures are detected in both devices.

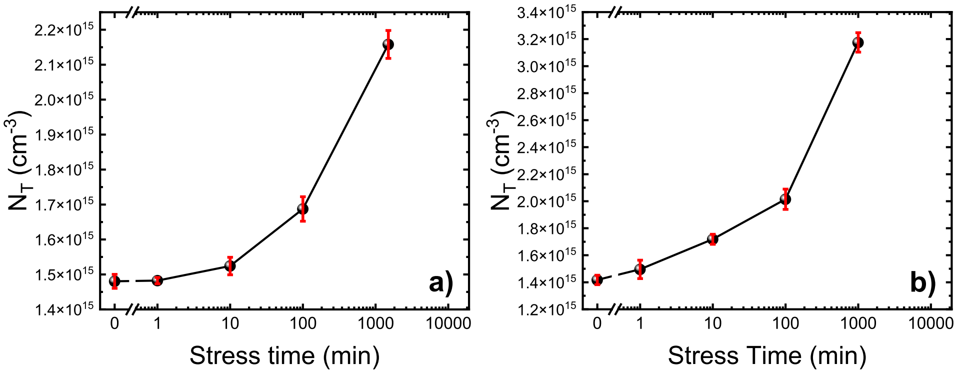

Fig. 11. Trap density comparison: a) on-target device, b) on-source device. The values indicate the total trap density, that is the sum of trap density T_1 and T_2.

8. Conclusions

In this work we analyzed impact of annealing on the optical and electrical characteristics of heterogeneously integrated C-band laser diodes integrated on silicon photonics. The reduction in resistance is accompanied by an increase in threshold. This threshold increase is attributed to Zn-related defects that diffuse towards the active region, increasing the number of non-radiative recombination centers. We also compared devices originating from the same epitaxial wafer that underwent identical fabrication steps, with the only difference being that one batch was micro-transfer printed onto silicon, while the other was characterized on the native substrate. Both sets exhibited the same defect levels, with comparable variations in defect concentration. This demonstrates that the micro-transfer printing process is not responsible for the observed changes in optical characteristics.

In order to mitigate this effect, the Zn doping profile could be optimized to minimize the impact of the diffusion, diffusion blocking layers could be incorporated in the III-V layer stack [31,32] or carbon could be used as a p-type dopant, which has been reported to exhibit a lower diffusion coefficient in InP than zinc [33].

Funding. PhotonixFAB, Dutch National Growth Fund PhotonDelta, PHORMIC.

Disclosures. The authors declare no conflicts on interest.

Data availability. Data underlying the results presented in this paper are not publicly available at this time but may be obtained from the authors upon reasonable request.

References

1. J. Meng, M. Miscuglio, J. K. George, *et al.*, "Electronic Bottleneck Suppression in Next-Generation Networks with Integrated Photonic Digital-to-Analog Converters," Adv. Photonics Res **2**(2), 2170004 (2021).
2. N. Margalit, C. Xiang, S. M. Bowers, *et al.*, "Perspective on the future of silicon photonics and electronics," Appl. Phys. Lett **118**(22), 220501 (2021).
3. A. Rahim, J. Goyvaerts, B. Szelag, *et al.*, "Open-access silicon photonics platforms in Europe," IEEE J. Sel. Top. Quantum Electron. **25**(5), 1–18 (2019).
4. T. Trupke, M. A. Green, and P. Würfel, "Optical gain in materials with indirect transitions," J. Appl. Phys **93**(11), 9058–9061 (2003).
5. C. S. C. Barrett, A. Atassi, E. L. Kennon, *et al.*, "Dissolution of antiphase domain boundaries in GaAs on Si(001) via post-growth annealing," J. Mater. Sci **54**(9), 7028–7034 (2019).
6. D. Jung, R. Herrick, J. Norman, *et al.*, "Impact of threading dislocation density on the lifetime of InAs quantum dot lasers on Si," Appl. Phys. Lett **112**(15), 153507 (2018).
7. J. Selvidge, J. Norman, E. T. Hughes, *et al.*, "Defect filtering for thermal expansion induced dislocations in III-V lasers on silicon," Appl. Phys. Lett **117**(12), 122101 (2020).
8. J. C. Norman, D. Jung, Y. Wan, *et al.*, "Perspective: The future of quantum dot photonic integrated circuits," APL Photonics **3**(3), 030901 (2018).
9. P. Y. Hsieh, A. Ben Driss, A. Tsiara, *et al.*, "Modeling Dark Current Degradation of Monolithic InGaAs/GaAs-On-Si Nano-Ridge Photodetectors," in *IEEE International Reliability Physics Symposium Proceedings* (Institute of Electrical and Electronics Engineers Inc., 2024).
10. A. W. Fang, H. Park, O. Cohen, *et al.*, "Electrically pumped hybrid AlGaInAs-silicon evanescent laser," Opt. Express **14**(20), 9203 (2006).
11. A. Moscoso-Mártir, F. Merget, J. Mueller, *et al.*, "Hybrid silicon photonics flip-chip laser integration with vertical self-alignment," in *2017 Conference on Lasers and Electro-Optics Pacific Rim, CLEO-PR 2017* (Institute of Electrical and Electronics Engineers Inc., 2017), Vol. 2017-Janua, pp. 1–4.
12. G. Roelkens, J. Zhang, L. Bogaert, *et al.*, "Micro-Transfer Printing for Heterogeneous Si Photonic Integrated Circuits," IEEE J. Sel. Top. Quantum Electron. (2022).
13. G. Roelkens, J. Zhang, L. Bogaert, *et al.*, "Present and future of micro-transfer printing for heterogeneous photonic integrated circuits," APL Photonics **9**(1), 010901 (2024).
14. E. Soltanian, G. Muliuk, S. Uvin, *et al.*, "Micro-transfer-printed narrow-linewidth III-V-on-Si double laser structure with a combined 110 nm tuning range," Opt. Express **30**(22), 39329 (2022).
15. Y. Lv, H. Tang, B. Han, *et al.*, "Properties of Au/Pt/Ti contact to p-InP by rapid thermal processing," Infrared Materials, Devices, and Applications **6835**, 68350D (2007).
16. G. Stareev, H. Künzel, and G. Dortmann, "A controllable mechanism of forming extremely low-resistance nonalloyed ohmic contacts to group III-V compound semiconductors," J. Appl. Phys **74**(12), 7344–7356 (1993).
17. C. He, H. R. Kunz, J. M. Fenton, *et al.*, *Comparison of Ti/Pt/Au and Ti/Ru/Au Contact Systems to p-Type InGaP* (1997), Vol. 12.
18. L. A. Coldren, S. W. Corzine, and M. L. Mashanovich, *Diode Lasers and Photonic Integrated Circuits* (Wiley, 2012), Chap. 2.
19. P. M. Mooney, "Chapter 2 Defect Identification Using Capacitance Spectroscopy," Semicond. Semimetals **51**, 93–152 (1999).
20. D. V. Lang, "Deep-level transient spectroscopy: A new method to characterize traps in semiconductors," J. Appl. Phys **45**(7), 3023–3032 (1974).
21. W. Chen, *Deep Level Defects in Indium Phosphide PIN Diodes*, University of Notre Dame, (2011).
22. S. I. Radautsan, I. M. Tiginyanu, V. V. Ursakii, *et al.*, *Subject Classification: 71.55; S7.11 Institute of Applied Physics* (1989), Vol. 115.
23. V. Janardhanam, A. Ashok Kumar, V. Rajagopal Reddy, *et al.*, "Study of deep level defect behavior in undoped n-InP (1 0 0) after rapid thermal annealing," in Microelectronic Engineering **88**(4), 506–508 (2011).
24. R. J. Walters and G. P. Summers, "Deep level transient spectroscopy study of proton irradiated p-type InP," J. Appl. Phys **69**(9), 6488–6494 (1991).
25. T. K. Oanh Vu, M. T. Tran, N. X. Tu, *et al.*, "Electronic transport mechanism and defect states for p-InP/i-InGaAs/n-InP photodiodes," J. Mater. Res. Technol. **19**, 2742–2749 (2022).
26. S. W. S. McKeever, R. J. Walters, S. R. Messenger, *et al.*, "Deep level transient spectroscopy of irradiated p-type InP grown by metalorganic chemical vapor deposition," J. Appl. Phys **69**(3), 1435–1439 (1991).
27. J. L. Benton, M. Levinson, A. T. MacRander, *et al.*, "Recombination enhanced defect annealing in n-InP," Appl. Phys. Lett **45**(5), 566–568 (1984).
28. A. Hierro, A. R. Arehart, B. Heying, *et al.*, "Capture Kinetics of Electron Traps in MBE-Grown n-GaN," physica status solidi (b) **228**(1), 309–313 (2001).
29. N. Otsuka, M. Kito, M. Ishino, *et al.*, "Control of double diffusion front unintentionally penetrated from a Zn doped InP layer during metalorganic vapor phase epitaxy," J. Appl. Phys **84**(8), 4239–4247 (1998).

Optics EXPRESS

30. M. Castleton and S. Mirbt, "Structure of the [ZnIn-VP] defect complex in Zn-doped InP," Phys. Rev. B Condens. Matter Mater. Phys **68**(8), 085203 (2003).
31. J. Cao, Y. Yu, T. Li, *et al.*, "Lightly doped In0.53Ga0.47As/InP SWIR photodetectors with diffusion barrier structure," Infrared Phys. Technol **137**, 105112 (2024).
32. S. P. Duggan, H. Yang, N. P. Kelly, *et al.*, "P-substrate InP-based 1.5 µm lasers using an internal carbon- doped layer to block p-dopant diffusion," Microw. Opt. Technol. Lett **60**(10), 2363–2367 (2018).
33. T. Teng, A. Xu, L. Ai, *et al.*, "InP/InGaAs/InP DHBT structures with high carbon-doped base grown by gas source molecular beam epitaxy," J. Cryst. Growth **378**, 618–621 (2013).